Publ. Astron. Soc. Japan (2019) 71 (SP1), S1 (1–14)
doi: 10.1093/pasj/psy094
Advance Access Publication Date: 2018 September 13

FOREST Unbiased Galactic Plane Imaging Survey with the Nobeyama 45 m telescope (FUGIN). IV. Galactic shock wave and molecular bow shock in the 4 kpc arm of the Galaxy

Yoshiaki Sofue,[1,*] Mikito Kohno,[2] Kazufumi Torii,[3] Tomofumi Umemoto,[3] Nario Kuno,[4,5] Kengo Tachihara,[2] Tetsuhiro Minamidani,[3,6] Shinji Fujita,[2,3,5] Mitsuhiro Matsuo,[3,7] Atsushi Nishimura,[2] Yuya Tsuda,[8] and Masumichi Seta[9]

[1]Institute of Astronomy, The University of Tokyo, 2-21-1 Osawa, Mitaka, Tokyo 181-0015
[2]Department of Physics, School of Science, Nagoya University Furo-cho, Chikusa-ku, Nagoya, Aichi 464-8602, Japan
[3]Nobeyama Radio Observatory, NAOJ, 462-2 Nobeyama, Minamimaki, Minamisaku, Nagano 384-1305, Japan
[4]Department Physics, Graduate School of Pure and Applied Sciences, University of Tsukuba, 1-1-1 Tenodai, Tsukuba, Ibaraki 305-8571, Japan
[5]Tomonaga Center for the History of the Universe, University of Tsukuba, 1-1-1 Tenodai, Tsukuba, Ibaraki 305-8571, Japan
[6]Department of Astronomical Science, School of Physical Sciences, The Graduate University for Advanced Studies, 2-21-1 Osawa, Mitaka, Tokyo 181-8588, Japan
[7]Graduate School of Science and Engineering, Kagoshima University, 1-21-40 Korimoto, Kagoshima-city, Kagoshima 890-0065, Japan
[8]Department of Physics, School of Science and Engineering, Meisei University, 2-1-1 Hodokubo, Hino-shi, Tokyo 191-8506, Japan
[9]Department of Physics, Kwansei Gakuin University, 2-1 Gakuen, Hyogo 669-1337, Japan

*E-mail: sofue@ioa.s.u-tokyo.ac.jp

Received 2018 May 29; Accepted 2018 July 17

Abstract

The FUGIN CO survey revealed the three-dimensional structure of a galactic shock wave in the tangential direction of the 4 kpc molecular arm. The shock front is located at G30.5+00.0 + 95 km s^{-1} on the upstream (lower longitude) side of the star-forming complex W 43 (G30.8−0.03), and comprises a molecular bow shock (MBS) concave to W 43, exhibiting an arc-shaped molecular ridge perpendicular to the galactic plane with width $\sim 0.^{\circ}1$(10 pc) and vertical length $\sim 1^{\circ}$ (100 pc). The MBS is coincident with the radio continuum bow of thermal origin, indicating association of ionized gas and similarity to a cometary bright-rimmed cloud. The upstream edge of the bow is sharp, with a growth width of $\sim$0.5 pc indicative of the shock front property. The velocity width is $\sim$10 km s^{-1}, and the center velocity decreases by $\sim$15 km s^{-1} from the bottom to the top of the bow.

The total mass of molecular gas in the MBS is estimated to be $\sim 1.2 \times 10^6\,M_\odot$, and ionized gas $\sim 2 \times 10^4\,M_\odot$. The vertical disk thickness has a step-like increase at the MBS by $\sim$2 times from lower to upper longitudes, which indicates hydraulic jump in the gaseous disk. We argue that the MBS was formed by the galactic shock compression of an accelerated flow in the spiral-arm potential encountering the W 43 molecular complex. A bow-shock theory can reproduce the bow morphology well. We argue that molecular bows are common in galactic shock waves, not only in the Galaxy but also in galaxies, where MBSs are associated with giant cometary H II regions. We also analyzed the H I data in the same region to obtain a map of H I optical depth and molecular fraction. We found firm evidence of the H I to H_2 transition in the galactic shock as revealed by a sharp molecular front at the MBS front.

Key words: Galaxy: disk — Galaxy: kinematics and dynamics — ISM: molecules — shock waves

1 Introduction

A galactic bow shock was observed in the tangential direction at G30.5+00 of the 4 kpc molecular arm (Scutum arm) in radio continuum emission at 10 GHz using the Nobeyama 45 m telescope (Sofue 1985), which revealed a cross-section of the gaseous spiral arm. The radio bow shock showed a concave arc with respect to the star-forming (SF) region W 43 at G30.8−0.03. (Hereafter, G$l \pm b$ represents the position or name of the object centered at l and b in degrees.)

From the concave structure, it was interpreted as due to a bow shock produced by a supersonic flow of interstellar gas encountering the massive molecular complex around W 43. A molecular arc in the ^{12}CO(J = 1–0) line at $v_{\rm LSR}$ = 90–100 km s^{-1} was also found to be associated with the radio bow shock using earlier low-resolution CO observations. The molecular clouds and bow shock G30.5 are considered to be located near the tangent point of the 4 kpc arm (Scutum arm) outside the supposed Galactic bar.

Astrophysical bow shock is a classical subject, and is commonly observed associated with objects interacting with supersonic flows. There have been a number of observations and models in various-scaled objects, from the geomagnetosphere in the solar wind (Baranov et al. 1971), interstellar globules against interstellar medium (ISM) flow and a UV field (Dyson et al. 1975), shocks in H II regions (van Buren et al. 1990; Povich et al. 2008), stellar winds against ISM flow (Wilkin 1996; Ueta et al. 2008), stellar outflows and environment (Arce & Goodman 2002), and cosmic jets against the ambient medium (Ogura 1995; Reipurth et al. 2002; Sakemi et al. 2018).

In this paper we revisit the galactic bow shock G30.5+00 in the 4 kpc arm (Scutum arm), and study its detail using the most recent CO-line observations. We model the bow shock as due to supersonic flow of gas in the galactic shock wave encountering the star-forming complex W 43. We argue that the galactic-arm-scale bow shock is a common phenomenon in spiral arms of galaxies observed as giant cometary H II regions. We discuss these topics based on the galactic shock wave theory (Fujimoto 1968; Roberts 1972; Tosa 1973).

As to the SF activity in the W 43 region, a number of papers have been published based on observations from radio to infrared emissions (Subrahmanyan & Goss 1996; Bally et al. 2010; Nguyen Luong et al. 2011; Beuther et al. 2012; Carlhoff et al. 2013; Motte et al. 2014; Bihr et al. 2015; Saral et al. 2017). The FUGIN CO survey has provided higher resolution and more sensitive maps in the CO lines in a wide field around W 43, and revealed detailed structures and kinematics of the molecular complex associated with W 43. Results of full analyses of the FUGIN data of the W 43 region are presented in M. Kohno et al. (in preparation) along with a detailed study of SF activity.

For this analysis, we use the ^{12}CO(J = 1–0) line data from the FUGIN CO-line survey (Umemoto et al. 2017; Kohno et al. 2018). The data cubes covered the Galactic plane region around W 43 from $l = 29^\circ$ to 32° and $b = -1^\circ$ to $+1^\circ$ from FUGIN, with spatial and velocity resolutions of $20'' \times 20'' \times 0.65$ km s^{-1}. We use only the ^{12}CO(J = 1–0) data because the extended molecular feature is more clearly observed than other CO lines and the mass estimation will be made using the CO to H_2 conversion factor available only for ^{12}CO(J = 1–0).

Very long baseline interferometry parallax measurements of maser sources (Zhang et al. 2014; Sato et al. 2014) in the G31.5 and G29.96 SF regions (not W 43 Main at G30.8) indicated a mean distance of $r \sim 5.5$ kpc. This distance agrees with a near-side kinematical distance corresponding to $v_{\rm LSR} \sim 95$ km s^{-1} at $l \sim 30.^\circ 8$ for the galactic rotation velocity (Sofue 2013) with $V \simeq 225$ km s^{-1} at $l \sim 30^\circ$ and solar constant of $V_0 = 238$ km s^{-1} (Honma et al. 2015). We adopt this distance for W 43 and

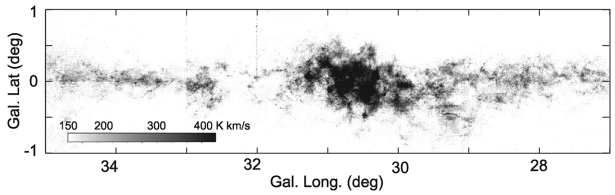

Fig. 1. ^{12}CO(J = 1–0) intensity map integrated from $v_{\rm LSR} = -20$ to +160 in the tangential direction of the 4 kpc arm around W 43 (G30.8).

the associated molecular clouds at $v_{\rm LSR} \sim 95\,{\rm km\,s^{-1}}$, as well as the galactic bow shock G30.5+00. We assume a galactocentric distance of the Sun of $R_0 = 8.0$ kpc, which locates W 43 at a galactocentric distance of 4.3 kpc at an azimuthal angle of 40°.6.

2 The maps

2.1 Continuum, CO and H I maps

Figure 1 shows an integrated intensity map of the ^{12}CO(J = 1–0) line emission of the Galactic plane at $l = 27°$ to 35° integrated at $v_{\rm LSR} = -20$ to $160\,{\rm km\,s^{-1}}$. The tangential direction of the 4 kpc arm (Scutum arm) including the star-forming complex W 43 is visible as a large clump around G31, showing the cross-section of the arm. The gray scaling starts at $I_{\rm CO} = 150\,{\rm K\,km\,s^{-1}}$, so that the map represents relatively high column regions near the tangent points of the galactic rotation.

In figure 2 we compare the CO map around W 43 with those in the radio continuum and for the H I line. The radio continuum map at 10 GHz observed with the Nobeyama 45 m telescope (Sofue 1985; Handa et al. 1987) in figure 2a reveals the radio bow shock as a vertical arc extending from G30.5+00 toward both latitudes up to $b \sim \pm 0°.7$–0°.8. The arc is concave to the strong radio source W 43 Main at G30.8−0.03. The dashed line traces the sharpest CO ridge recognized in the CO channel map at $v_{\rm LSR} = 95\,{\rm km\,s^{-1}}$.

Figures 2b and 2c show a CO channel map at $v_{\rm LSR} = 95\,{\rm km\,s^{-1}}$ and intensity integrated from $v_{\rm LSR} = 85$ to $105\,{\rm km\,s^{-1}}$ with cutting flux at 2 K. Three dense molecular regions are evident at G30.0 near the compact H II region G29.96 (W 43 West), G30.5 (molecular bow shock), and G30.8 (W 43 Main). Besides these clouds, vertically extended arcs are visible at G30.0, G30.5, and G31.6, particularly prominent at G30.5. We focus on this long arc at G30.5, and call it the molecular bow shock (MBS) G30.5. The MBS positionally coincides with the radio continuum bow, extending toward latitudes $b \sim \pm 0°.8$, and is concave to W 43.

Figure 2d shows the optical depth map of the 21 cm H I line for averaged brightness temperature between 85 and $105\,{\rm km\,s^{-1}}$ for an assumed spin temperature of 130 K, as obtained using the THOR H I survey by Bihr et al. (2015). A significantly deficient region of H I appears around G30.5 in positional coincidence with the molecular bow. In the channel maps of H I emission, this deficiency is visible in the velocity range from 90 to $100\,{\rm km\,s^{-1}}$, close to that of the MBS. The velocity-selected deficiency confirms that the H I deficiency is not due to absorption against the continuum background, but H I gas is really less abundant in this velocity range. This feature will be discussed in relation to H I to H_2 transition in section 5.

2.2 Molecular gas components

We categorize the molecular structures in the analyzed region into four components using the integrated intensity map in analogy to usual ISM terms: (i) giant molecular association (GMA), (ii) giant molecular clouds (GMC), (iii) dense molecular clouds (DMC), and (iv) molecular cores. We define these four components as clouds in regions enclosed by contours at threshold intensities at $I_{\rm c}$ = 100, 200, 300, and $400\,{\rm K\,km\,s^{-1}}$, respectively, in the ^{12}CO(J = 1–0) intensity map integrated between $v_{\rm LSR} = 80$ and $120\,{\rm km\,s^{-1}}$ shown in figure 2c.

The mass of each component is measured by surface integration of the intensity enclosed by the threshold contours at $I_{\rm CO} = I_{\rm c}$ as

$$M = X_{\rm mass} \int I_{\rm CO}(\geq I_{\rm c}) dx dy, \quad (1)$$

where $X_{\rm mass}$ is the CO to H_2 conversion factor, dx and dy are linear extents in the l and b directions, and we assume a distance of 5.5 kpc. We adopt a conversion factor for the ^{12}CO(J = 1–0) line, $X_{\rm CO} = 2.0 \times 10^{20}\,{\rm H_2\,cm^{-2}\,[K\,km\,s^{-1}]^{-1}} = 3.20\,M_\odot\,{\rm pc^{-2}\,[K\,km\,s^{-1}]^{-1}}$, which yields $X_{\rm mass} = 4.3\,M_\odot\,{\rm pc^{-2}\,[K\,km\,s^{-1}]^{-1}}$ including heavy elements (Bolatto et al. 2013). We list the calculated masses in table 1.

It may be stressed that the mass of individual GMCs estimated here, $M \sim 1.5 \times 10^6\,M_\odot$ (see below), is comparable to that of the usual GMC. It should also be noted that the mass of the cores $\sim 1.6 \times 10^5\,M_\odot$ in diameter of ∼8 pc is consistent with that obtained for the W 43 Main+West clouds of $\sim 2 \times 10^5\,M_\odot$ in $\sim 20 \times 10\,{\rm pc^2}$ from dust emission (Lin et al. 2016).

As for sizes, we define the representative diameter (size) and radius, $D = 2a$, by $A = \pi a^2 = \pi D^2/4$, where A is the area enclosed by the threshold contours in figure 2c. In table 1 we list the measured values, where $I_{\rm c}$ is the threshold intensity and $\langle I_{\rm c} \rangle$ is the averaged intensity in area A.

We also estimate the gravitational energy by $E_{\rm g} = GM^2/a$, assuming that the line-of-sight extent is equal to the diameter, where G is the gravitational constant. We

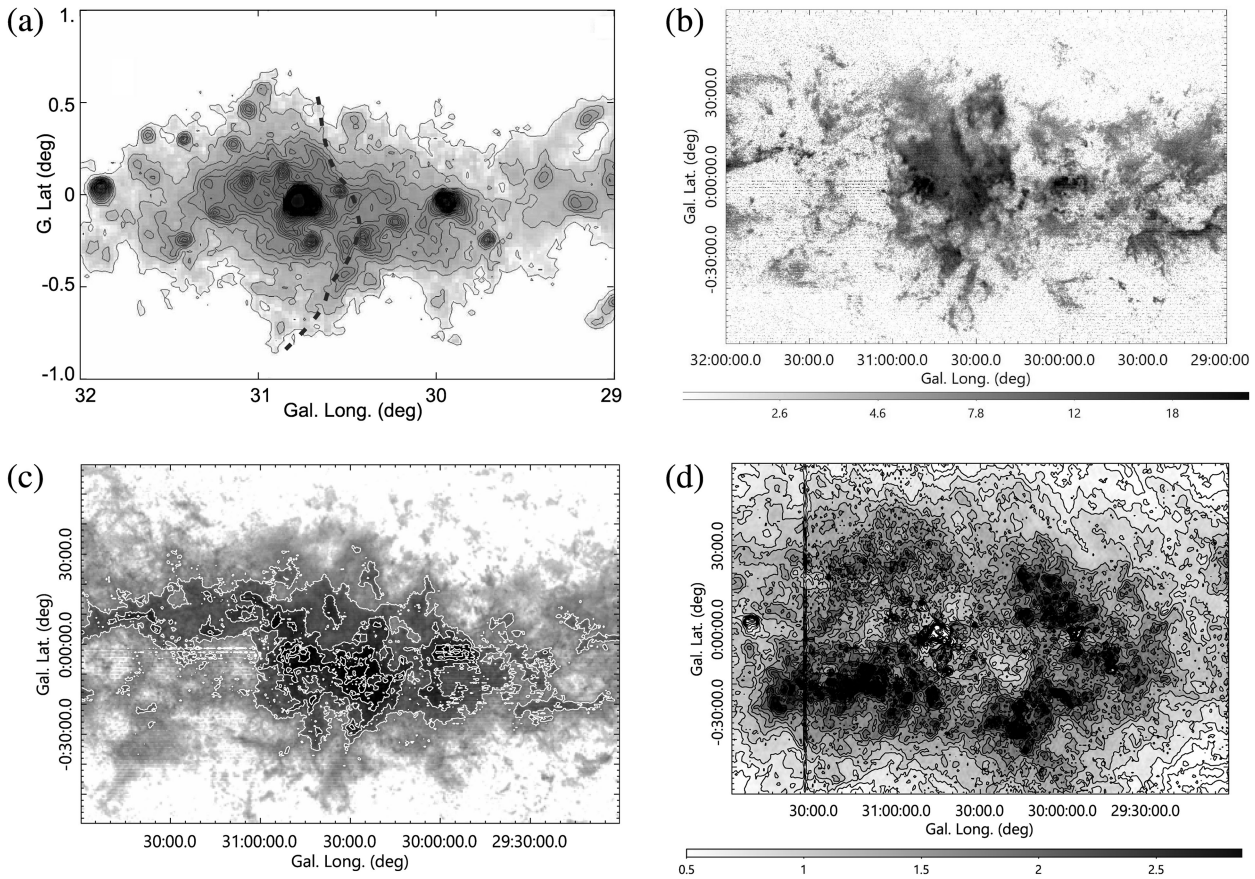

Fig. 2. (a) 10 GHz continuum map (Sofue 1985; Handa et al. 1987), showing H II regions W 43 Main (G35.8) and West (G29.96), and a radio bow shock at G30.5 concave to W 43 Main. The dashed line traces a molecular ridge in (b). (b) Channel map of ^{12}CO($J = 1$–0) line at $v = 94.465\,\mathrm{km\,s^{-1}}$. (c) ^{12}CO($J = 1$–0) integrated intensity map from $v_{\mathrm{LSR}} = 80$ to 120 km s^{-1}. The contours are at $I_{\mathrm{c}} = 100\,\mathrm{K\,km\,s^{-1}}$ (approximately the surrounding GMA, see text), 200 (GMC), 300 (DMC), and 400 K km s^{-1} (cores). The horizontal stripes at $l > 31^{\circ}$ and $b < 0^{\circ}$ are instrumental artifacts. (c) H I optical depth, $\tau_{\mathrm{H\,I}}$, calculated for averaged T_{B} at $v_{\mathrm{LSR}} = 85$ to 105 km s^{-1} from the THOR H I survey by Bihr et al. (2015). Values toward strong continuum sources brighter than $T_{\mathrm{S}} = 130$ K (W 43, G29.96, etc.) are not valid. The vertical stripe at $l = 30.^{\circ}1$ is an artifact.

compare it with the kinetic energy $E_{\mathrm{g}} \sim M\sigma_v^2/2$ in order to confirm that $E_{\mathrm{g}}/E_{\mathrm{k}} > 1$ so that the clouds are gravitationally bound. The velocity dispersion was estimated by $\sigma_v \sim \sqrt{2}w$, where w is the velocity width in the moment-2 map. Using figure 3b we estimate the widths as $w \sim 5\,\mathrm{km\,s^{-1}}$ for the GMA, $\sim$6 km s^{-1} for the GMC, and $\sim$8 for the DMC and cores, and hence $\sigma_v \sim 7$, 8.4, and 11 km s^{-1}, respectively. The mass is further used to calculate the density by $\rho = M/(4\pi a^3/3)$, and the Jeans time $t = 1/\sqrt{G\rho}$ (timescale of gravitational contraction). In table 1 we list the calculated values for individual components.

If there exist N clouds in the analyzed field, the individual diameter of each component is given by $D' \sim D/\sqrt{N}$. Accordingly, the mass of a single typical cloud is estimated by $M' \sim M/N$. As the total gravitational energy is overestimated by a factor of $\sim \sqrt{N}$, the individual energy is reduced to E'_{g} and related to E_{g} by $E'_{\mathrm{g}} \sim E_{\mathrm{g}}/\sqrt{N}$. Similarly, the individual density ρ' and Jeans time t' are approximated by the calculated density and time by $\rho' \sim \sqrt{N}\rho$ and $t' \sim N^{-1/4}t$. Estimating by eye in figure 2c, we counted the numbers of clouds to be $N \sim 1$ for the GMA and $\sim$3 for the GMC, DMC, and cores.

2.3 Kinematical properties

Figures 3a and 3b show moment-1 and -2 maps, showing the intensity-weight velocity field and velocity width distributions, respectively. The velocity field shows systematic variation with longitude. It shows a rapid decrease in velocity at G30.5, with gradient much steeper than the decrease due to the Galactic rotation, indicating sudden deceleration of gas near G30.5.

Although it shows the general variation of velocities, the moment-1 map is contaminated by widely extended components at velocities between 80 and 120 km s^{-1}. In order to examine the velocity structure more specifically for the MBS, we made a color-coded intensity map around G30.5

Table 1. Sizes, masses, energies, and Jeans times of molecular clouds calculated for $\sigma_v = 10\,\mathrm{km\,s^{-1}}$.*

Compo.†,‡	I_c (K km s^{-1})	$\langle I_c \rangle$ (K km s^{-1})	D (pc)	M ($M_\odot$)	σ_v (km s^{-1})	log E_g (erg)	log E_k (erg)	E_g/E_k	n_{H_2} (H_2 cm^{-3})	t (Myr)
GMA	100.0	168.3	120.7	0.13E+08	7	53.29	51.81	29.9	0.11E+03	5.53
H I§	—	—	—	0.17E+07	—	—	—	—	0.75E+02 H	—
GMC	200.0	259.2	58.0	0.47E+07	8.5	52.71	51.52	15.3	0.35E+03	3.09
DMC	300.0	345.0	25.6	0.12E+07	11	51.89	51.19	5.1	0.10E+04	1.78
Core	400.0	458.5	8.2	0.16E+06	11	50.65	50.32	2.2	0.44E+04	0.87
MBS			Vol. (pc^3)							
Mol.	—	150	$100^2 \times 10$	0.12E+07	—	—	—	—	0.13 E+03	—
H II	—	—	—	0.20 E+05	—	—	49.5 (th.)	—	8 H	—

*$X_{mass} = 4.3\,M_\odot\,\mathrm{pc^{-2}}\,[\mathrm{K\,km\,s^{-1}}]^{-1}$ (including heavy elements: 1.36 times the H_2 mass for $X_{CO} = 2.0 \times 10^{20}\,H_2\,\mathrm{cm^{-2}}\,[\mathrm{K\,km\,s^{-1}}]^{-1}$).
†GMA: giant molecular association; GMC: giant molecular cloud; DMC: dense molecular cloud; MBS: molecular bow shock.
‡Mean values for each component can be estimated by $D' \sim D/\sqrt{N}$, $M' \sim M/N$, $E'_g \sim E_g/\sqrt{N}$, $\rho' \sim \sqrt{N}\rho$, and $t' \sim N^{-1/4}t$ (not listed here), where $N \sim 1$ for GMA and ∼3 for GMC and DMC/cores.
§H I mass $\sim A \times \Sigma_{H1}$, where $\Sigma_{H1} \sim 150\,M_\odot\,\mathrm{pc^{-2}} \simeq 1.9 \times 10^{22}\,\mathrm{H\,cm^{-2}}$ (Bihr et al. 2015).

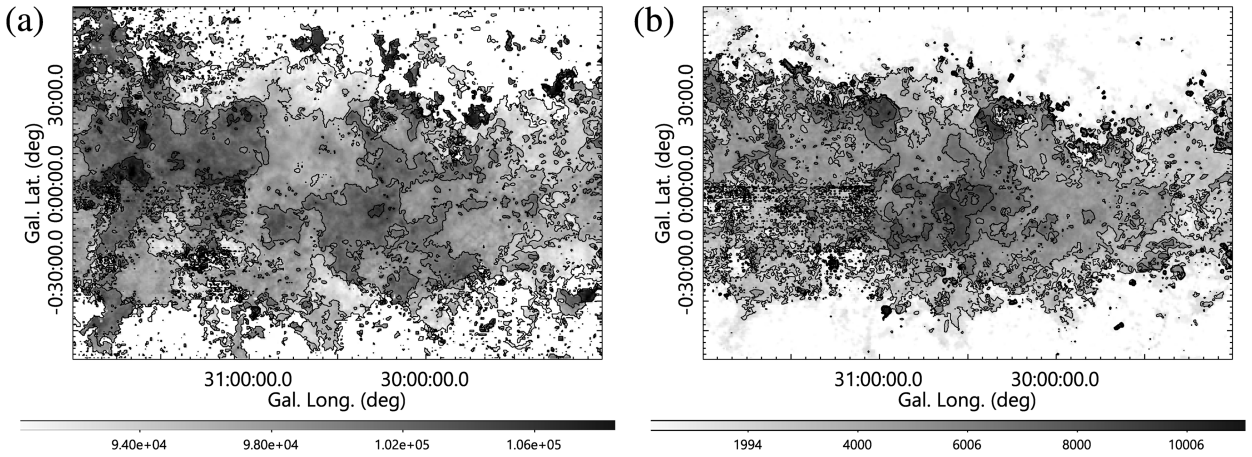

Fig. 3. (a) Moment 1 (velocity field) map with contours every 5 km s^{-1}. Note the contours running almost vertically, showing systematic variation with longitude, but inversely against the galactic rotation near G30.5. (b) Moment-2 (velocity width) map with contours every 2 km s^{-1}.

using channel maps closer to the MBS's center velocity at 91, 95, and 99 km s^{-1} in blue, green, and red, respectively.

The G30.8+00 molecular complex associated with the H II region W 43 is kinematically located near the tangent point along the 4 kpc molecular arm (Scutum arm) at radial velocity slightly slower than the terminal velocity. Figure 4a shows an LV diagram at $b = -0.^\circ25$, where the velocity of the molecular gas around the MBS changes drastically from lower to upper longitudes, as indicated by the thick dashed line. Figure 4b shows the variation of the intensity-weighted mean v_{LSR} (moment-1, as in figure 3) at the same latitude from $l = 30^\circ$ to 31°, showing a sudden decrease in the radial velocity at the MBS (arrow). The velocity variation is much steeper than expected from the terminal velocity due to the Galactic rotation, as shown by the thin dashed line.

In order to separate the kinematical behaviors from the surrounding clouds, we made velocity–latitude diagrams at different longitudes around the MBS. The MBS gas is extended in the latitude direction for more than $\pm0.^\circ9$ (90 pc), or further beyond the observed edges. Impressive in the VB diagrams is the bow-like edge of the $v - b$ profile concave to the W 43 molecular complex in the highest brightness region. We show a $v - b$ diagram at $l = 37.^\circ5$ in figure 5.

Combining these kinematical behaviors in the $v - b$ diagrams with the geometrical and morphological considerations in the previous section, we may summarize the three-dimensional kinematical structure of the molecular bow shock as illustrated in figure 5.

3 Three-dimensional molecular structure

3.1 Molecular bow

In the ^{12}CO($J = 1$–0) intensity map, the MBS is recognized as the vertical molecular arc extending from G30.5+00 toward both sides of the Galactic plane. The bow is concave

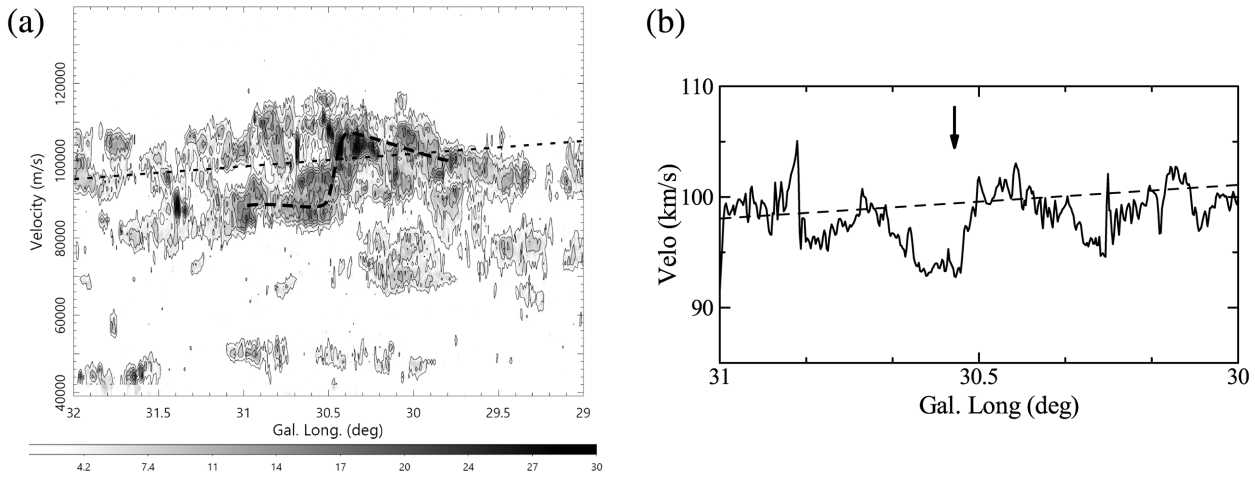

Fig. 4. (a) LV diagram at $b = -0.^{\circ}25$. The contours are drawn every 3 K, starting at 3 K. The thick and thin dashed lines indicate the trace of the velocity jump from up- to downstream side of the bow, and the terminal velocity expected from the galactic rotation, respectively. (b) Variation of intensity-weighted mean $v_{\rm LSR}$ along $b = -0.^{\circ}25$, showing sudden deceleration of radial velocity at the MBS (arrow). The dashed line represents the smoothed galactic rotation curve.

with respect to W 43 Main, and is visible in a narrow range of velocities from $v_{\rm LSR} \sim 90$ to 100 km s^{-1}, having a full velocity width of $\sim$10 km s^{-1}.

The extent of the MBS is $\Delta l \times \Delta b \sim 0.^{\circ}1 \times 1^{\circ}$, which corresponds to $L \times W \sim 10\,{\rm pc} \times 100\,{\rm pc}$ for an assumed distance of 5.5 kpc, where L is the vertical length and W is the width. From the figures we estimate the mean intensity along the MBS to be $I_{\rm CO} \sim 150\,{\rm K\,km\,s^{-1}}$, which yields the total mass of molecular gas in the bow shock to be $M_{\rm MBS} \sim 8.7 \times 10^5\,M_{\odot}$. This shares about $\sim$0.19 of the total GMC mass around W 43 of $\sim 4.7 \times 10^6\,M_{\odot}$ in table 1.

Figure 6 shows the horizontal variations of the brightness temperature at $v = 94.675\,{\rm km\,s^{-1}}$ from G30 to G31 at two different latitudes, $b = -0.^{\circ}43$, 0°, and $+0.^{\circ}23$. The cross-sections of the MBS indicated by the arrows exhibits a sharp edge, with a sudden increase of the intensity from right to left. The edge's growth width is comparable to the observing resolution of 20″, or $\sim$0.5 pc (figure 6).

Such cross-sections are typical for shock wave compression. The bow-shaped sharp edge along the MBS may be the first clear evidence for a galactic shock wave in the Galaxy caused by a supersonic flow from the upstream side of the Galactic rotation toward the downstream side against the 4 kpc arm.

3.2 Bow shock theory

We point out that the radio continuum bow along the MBS is similar to sub-pc-scale bright-rimmed clouds (BRC) associated with thermal radio emission, where the ionization occurs due to UV photons from nearby forming stars (Sugitani et al. 1991; Thompson et al. 2004; Urquhart et al. 2006). Although the MBS is caused by an encounter with the supersonic flow in Galactic rotation, the similarity suggests that the MBS would be a giant bright-rimmed molecular cloud (GBRC) of spiral-arm scale.

Such an inside bright rim may indeed be the case in MBS G30.5, illuminated by UV photons from W 43. In fact, the 10 GHz radio continuum emission in MBS G30.5 (figure 2) is located slightly inside the molecular bow, and it is possible that the emission is a mixture of ionized gas heated by the shock wave from outside and that excited by W 43 from inside.

According to Wilkin's (1996) analytical model for stellar bow shock, the bow-front shape is expressed as follows:

$$Q(\phi) = R_{\rm S}\,{\rm cosec}\,\phi\sqrt{3(1-\phi\,\cot\phi)}, \tag{2}$$

where Q and ϕ are the radius and elevation angle of the front from the galactic plane, $R_{\rm S}$ is the stand-off distance defined as the distance of the front on the galactic plane from the central body responsible for triggering the shock wave. We consider here that $R_{\rm S}$ is approximated by the distance of the MBS at G30.5+00 from W 43.

The stand-off distance, $R_{\rm S}$, which is a representative radius of the bow shock, is related to the bow's parameters as follows, considering the balance of momentum injection from the central body and ram pressure by the inflowing gas from outside:

$$R_{\rm S} = \sqrt{\frac{\dot{m}_{\rm w} V_{\rm w}}{4\pi\rho V^2}}, \tag{3}$$

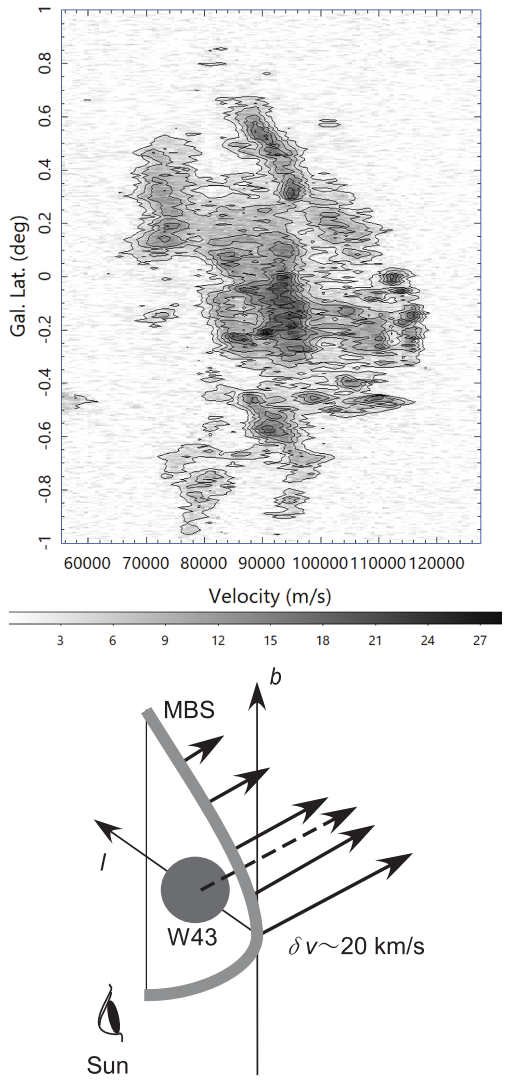

Fig. 5. (Top) Velocity–latitude diagram at G30.513. The contours are drawn every 3 K, starting at 3 K. (Bottom) Schematic view of relative line-of-sight motion of the MBS's tangent ridge.

where $\dot{m}$ is the mass injection rate into the shock front, and is approximated by

$$\dot{m} \sim M_{\rm MBS}/\tau. \quad (4)$$

Here, $\tau = d/V$ and $d \sim 10$ pc is the width of the MBS, $V_{\rm w}$ is the wind velocity from the central body, and is replaced by $V_{\rm w} \sim \sigma_v \sim 10\,{\rm km\,s^{-1}}$, and $\rho \sim 30\,{\rm H\,cm^{-3}}$ is the ambient gas density in the outskirts of the GMA taken as the logarithmic mean of the H I ($8\,{\rm H\,cm^{-3}}$) and molecular ($100\,{\rm H\,cm^{-3}}$) densities. The inflow gas velocity is given by $(V_{\rm rot} - V_{\rm p})\sin p \sim 30\,{\rm km\,s^{-1}}$, where $V_{\rm rot}$ and $V_{\rm p}$ are the rotation velocity and pattern speed of the spiral arm, respectively, and p is the pitch angle of the arm. Inserting these values into equation (3), we obtain $R_{\rm S} \sim 54$ pc.

In figure 7 we present the bow-shock shapes calculated for $R_{\rm S} = 25$, 50, and 75 pc overlaid on the ^{12}CO(J = 1–0) intensity map, where the curve for 50 pc represents the observed MBS shape well, in agreement with the above theoretical estimation of $R_{\rm S} \sim 54$ pc. We emphasize that the bow-shock model can represent the observed shapes and dimensions of the MBS well, if W 43 and its surrounding dense molecular cloud is the triggering source of the shock. Full discussion of the bow-shock formation mechanism in interstellar gas clouds in galactic spiral shock waves, including analyses of a number of dark-cloud bows found in nearby spiral galaxies, will be presented in a separate paper (Y. Sofue in preparation).

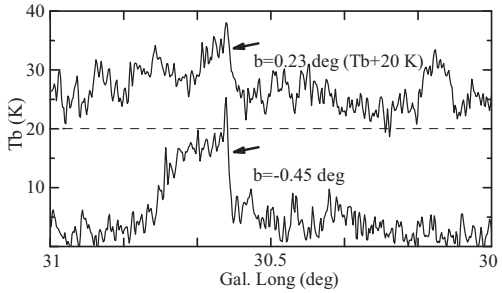

Fig. 6. Horizontal cuts of the CO-line brightness at $v = 95\,{\rm km\,s^{-1}}$ at $b = -0.^{\circ}45$ and $+0.^{\circ}23$. Note the sharp intensity rise at the western edge. The triangles indicate the longitudes of G29.96, G30.5, and W 43 Main.

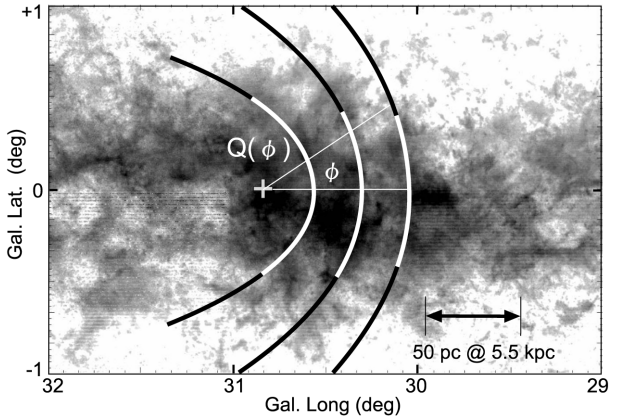

Fig. 7. Theoretical bow-shock front for standoff distance $R_{\rm S} = 25$, 50, and 75 pc centered on W 43 at $(X, Y) = (0, 0)$ pc, overlaid on the ^{12}CO($J = 1$–0) map.

3.3 Giant cometary H II region with bright rim

Figure 2 shows a positional coincidence of the 10 GHz continuum bow structure with the molecular bow at G30.5, while the continuum is slightly inside the MBS. The radio bow is also clearly visible on the 2, 7, and 5 GHz maps using the Bonn 100 m telescope (Altenhoff et al. 1979; Reich et al. 1990) and on the 330 MHz map by Subrahmanyan and Goss (1996) using the VLA. Spectral indices between 10 and 2.7 GHz indicate that the emission is thermal (Sofue 1985), which is also confirmed by comparing the 10 GHz

intensities with those at 330 MHz considering the missing flux in the VLA map.

The emission measure of the responsible ionized gas is estimated to be $EM \sim 7 \times 10^3\,\mathrm{pc\,cm^{-6}}$ for an assumed electron temperature of $T_e = 10^4$ K (Sofue 1985). The electron density is, then, estimated to be $n_e \sim 8\,\mathrm{cm^{-3}}$ for an assumed line-of-sight depth equal to the vertical extent of $L \sim 100$ pc. The H II mass is calculated to be $M \sim m_H n_e L^2 W \sim 2 \times 10^4\,M_\odot$, which is $\sim 3 \times 10^{-2}$ times the molecular mass. This yields the thermal energy density, or internal pressure, of the H II gas of $p_{int} \sim n_e k T_e \sim 1.1 \times 10^{-11}\,\mathrm{erg\,cm^{-3}}$.

We may consider two possible sources to ionize the gas in the continuum bow. One possible mechanism is ionization by UV illumination from inside by OB stars in W 43, and the other is shock-induced ionization by the inflowing supersonic flow by the Galactic shock wave.

The first, probably most likely, mechanism is ionization from inside (the downstream side) by UV photons from OB stars in W 43. This postulates the standard formation mechanism of an H II region around an OB star cluster. The radius of a steady-state (well-evolved) H II region is given by

$$R_{H\,II} \simeq \left(\frac{3 N_{UV}}{4\pi n_i n_e \alpha_r} \right)^{1/3}, \tag{5}$$

where N_{UV} is the UV photon number radiated by the OB stars and $\alpha_r \sim 4 \times 10^{-13}\,\mathrm{cm^3\,s^{-1}}$ is the recombination rate. If we assume that the luminosity of the central cluster is comparable to the far-infrared luminosity, $L \sim 1.23 \times 10^7\,L_\odot$, of dust clouds in the central 10 pc of W 43 (Lin et al. 2016), and that the ionized hydrogen density is $n_i \sim n_e \sim 8\,\mathrm{cm^{-3}}$ from the continuum EM, then we have $R_{H\,II} \sim 130$ pc.

Thus, W 43 is luminous enough to blow off most of the ambient H II gas to radius ~100 pc. However, the expanding H II gas is blocked by the dense molecular gas blowing from the upstream side in the Galactic shock wave. This counter-flow compresses the H II sphere to keep its radius smaller than $R_{H\,II}$. The observed standoff distance $R_S \sim 50$ of the MBS can thus be naturally explained by such a compressed radius of the H II region excited by W 43. On the contrary, on the downstream side of W 43 the gas flows away from W 43 causing suppressed ram pressure, so that the H II gas expands farther into the inter-arm region.

As a consequence, a giant cometary H II region showing a lopsided cone of ionized gas open to the downstream side is produced inside the MBS, as illustrated in figure 8. In fact, the radio continuum bow representing the H II rim is observed slightly inside the MBS in figure 2. We also

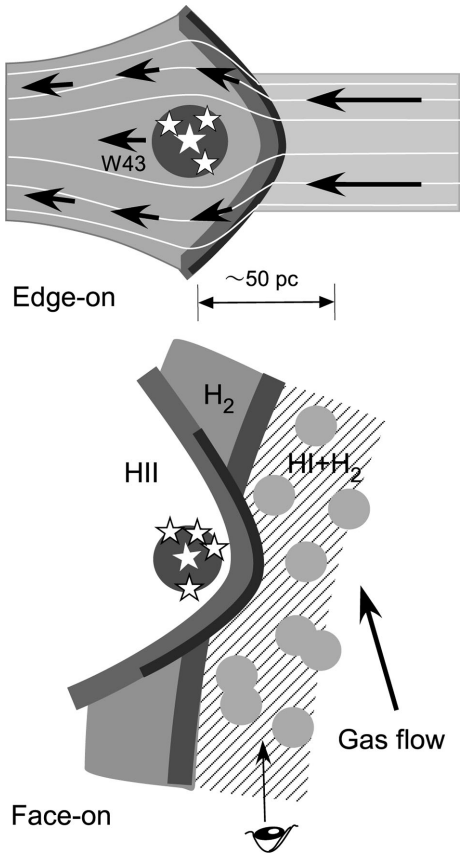

Fig. 8. (Top) Illustration of the cross-section and flow lines through the MBS. The arched shape is formed by the bow shock and hydraulic jump in the z direction. (Bottom) The same, but seen face-on. The molecular bow is formed around a giant cometary H II region, concave to the central OB stars. Similar dark bows and giant H II cones are commonly observed in star-forming spiral arms of external galaxies (Y. Sofue in preparation).

point out that similar giant cometary H II regions with Hα-bright rim are often observed in galactic shock wave arms of external galaxies (Y. Sofue in preparation).

Another hypothesis attributes the origin to ram pressure by the inflowing gas from the upstream side. The ram pressure is estimated to be $p_{ext} = m_H n_{pre} \Delta v^2 \sim 7 \times 10^{-11}\,\mathrm{erg\,cm^{-3}}$ for $\Delta v \sim 10\,\mathrm{km\,s^{-1}}$. Here, the pre-shock gas density was estimated by H I density observed toward ~G30.2+0.2 using the H I map by Bihr et al. (2015) to be $n_{pre} \sim N_{HI}/L \sim 40\,\mathrm{H\,cm^{-3}}$, where $L \sim 100$ pc is the line-of-sight depth and $N_{HI} \sim 100\,M_\odot\,\mathrm{pc^{-2}}$ is the H I column after subtraction of the extended background. Thus the inflowing gas pressure is sufficient to heat and partially ionize the gas at the bow shock. Note also that the pressure is comparable to the internal pressure by the molecular gas in the GMA of $p_{mol} \sim 2 m_H n_{H_2} \sigma_v^2/2 \sim 7 \times 10^{-11}\,\mathrm{erg\,cm^{-3}}$ for $\sigma_v \sim 10\,\mathrm{km\,s^{-1}}$, so that it can compress the molecular gas in the GMA stacked at the Galactic shock in the potential well.

The morphology of the MBS and continuum bow remind us of the cometary H II regions of parsec scales, which are considered to be produced by interaction of H II gas

expanding in inhomogeneous and/or flowing ISM (Reid & Ho 1985; van Buren et al. 1990; Arthur & Hoare 2006; Steggles et al. 2017). We also point out that the radio bow is similar to sub-parsec-scale bright-rimmed clouds, where the ionization occurs due to UV photons from nearby forming stars (Sugitani et al. 1991; Thompson et al. 2004; Urquhart et al. 2006). Although the present MBS is caused by an encounter with the supersonic flow in Galactic rotation, the similarity suggests that the MBS would be a giant cometary H II region with bright-rimmed molecular gas.

3.4 Hydraulic jump

Another feature to be stressed around MBS G30.5 is the sudden increase of vertical thickness of the disk from lower to higher longitudes (figures 1 and 2). Here, we define the thickness as an averaged separation of equal intensity contours at $I_{\rm CO} = 150\,{\rm K\,km\,s^{-1}}$ in the positive and negative latitudes in figure 1. Smoothing clumpy fluctuations, the upstream disk thickness at $l \leq 30^\circ$ is estimated to be $\Delta b \sim \pm 0.^\circ 5 \simeq 50$ pc. It then increases by a factor of $\sim$2 to $\pm 1^\circ \sim 100$ pc at $l = 30.^\circ 5$ in the 4 kpc arm, and returns to $\pm 0.^\circ 4$ (40 pc) at $l \geq 31^\circ$ in the outer inter-arm region.

The thickness jump may be attributed both to bow-shock effect by the supersonic flow as well as to a hydraulic jump from laminar to turbulent flow at the shocks. The height of the hydraulic jump z may be estimated by the change of the laminar flow's kinetic energy to turbulent energy, which is on the order of

$$z \sim \eta[(V_{\rm rot} - V_{\rm p})\ \sin\ p]^2/K_z, \qquad (6)$$

where the velocity term $\sim(V_{\rm rot} - V_{\rm p})\sin p$ is nearly equal to ΔV as observed. Here, η is the efficiency of conversion of laminar to turbulent kinetic energies, and K_z is the vertical acceleration by the disk's gravity.

If we adopt $V_{\rm rot} = 225\,{\rm km\,s^{-1}}$ at $R \sim 4$ kpc from the rotation curve (Sofue 2013) for $V_0 = 238\,{\rm km\,s^{-1}}$ (Honma et al. 2015), $V_{\rm p} \sim 100\,{\rm km\,s^{-1}}$ for an assumed pattern speed of $\Omega = 25\,{\rm km\,s^{-1}\,kpc^{-1}}$, $p \sim 11^\circ$ (Sofue & Nakanishi 2016), and $K_z = 0.76(z/100\,{\rm pc})\,({\rm km\,s^{-1}})^2\,{\rm pc^{-1}}$ (Kuijken & Gilmore 1989), and assume a conversion efficiency of $\eta \sim 0.5$, then we obtain $z \sim 100$ pc, sufficient to lift the laminar flow gas to the observed height of the MBS.

Variation of the disk thickness at a galactic shock wave has been investigated theoretically (Tosa 1973) and numerically by hydrodynamic simulations (Martos & Cox 1998; Gómez & Cox 2004a, 2004b), which showed a significant increase in the disk thickness by the hydraulic jump associated with vertically extended spur features. Although the simulations qualitatively explain the observed features, the current resolution, $\sim$0.1 kpc, is too crude to be compared with the present observation at much higher resolution, 15″ (0.4 pc). Quantitative comparison and more physical discussion such as to determine the efficiency η would be a subject for future simulations.

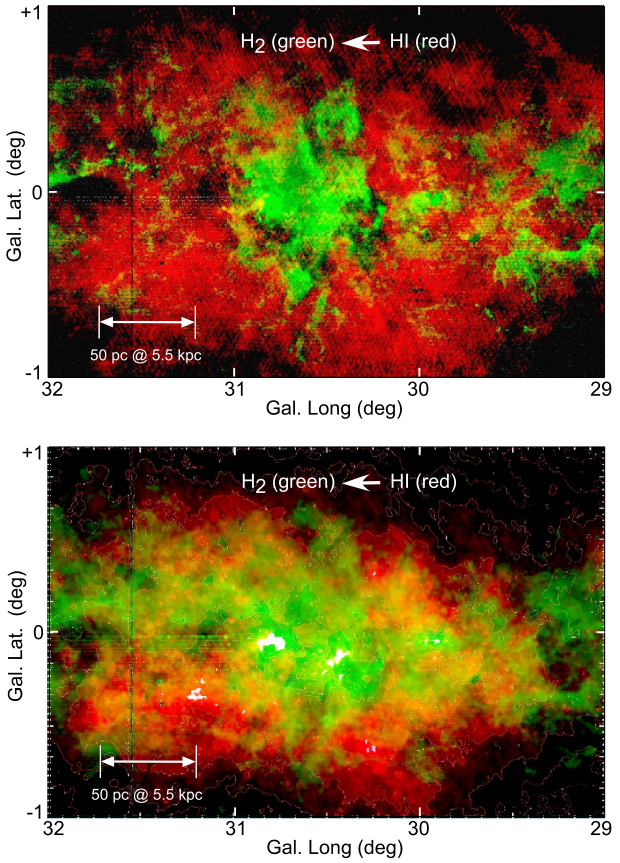

Fig. 9. (Top) ^{12}CO($J = 1$–0) brightness in green overlaid on H I brightness in red at $v_{\rm LSR} = 95\,{\rm km\,s^{-1}}$. (Bottom) $I_{\rm CO}$ (85 to 105 km s^{-1}) on $I_{\rm HI}$ in red, made from the THOR survey by Bihr et al. (2015). The intensity scales are arbitrary in order to compare the characteristic distributions in both lines. Note the deficiency of H I in CO-bright regions.

4 H I to H_2 transition in the Galactic shock: molecular front at the MBS front

Bialy et al. (2017) proposed an H I to H_2 transition scenario in the vicinity of W 43, comparing the H I and H_2 column densities from 21 cm line emission and far-infrared dust emission, respectively. Their scenario may be confirmed in a more specific way by slicing the intensities into velocity channels.

In figure 9 we overlay the channel maps at $v_{\rm LSR} = 95\,{\rm km\,s^{-1}}$ of ^{12}CO($J = 1$–0) brightness in green on that of H I in red, and ^{12}CO($J = 1$–0) intensity maps integrated from $v_{\rm LSR} = 85$ to 105 km s^{-1} on the H I intensity in the same velocity range as made from the THOR H I survey by Bihr et al. (2015). The figure shows that the CO strong regions are exactly located in the H I-deficient regions. Note that the

H I map is not corrected for absorption against continuum emission, but the absorption is significant only within ∼10′ of W 43 and compact H II regions.

We then investigate how the molecular gas is dominant in the region by mapping the molecular fraction defined by

$$f_{\rm mol} = \frac{2n_{\rm H2}}{2n_{\rm H2} + n_{\rm HI}}, \tag{7}$$

where $n_{\rm H_2}$ and $n_{\rm HI}$ are the densities of H_2 and H I. The densities are related to the observed brightness temperature through (Sofue 2018)

$$n_{\rm H_2} = X_{\rm CO}\, T_{\rm B:CO} \frac{dv}{dr} \tag{8}$$

and

$$n_{\rm HI} = X_{\rm HI} T_{\rm S} \tau_{\rm HI} \frac{dv}{dr}, \tag{9}$$

where the X_i are the conversion factors, and $\tau_{\rm HI}$ is the H I optical depth defined through

$$T_{\rm B:HI} = (T_{\rm S} - T_{\rm C})(1 - e^{-\tau_{\rm HI}}). \tag{10}$$

Here, $T_{\rm S}$ and $T_{\rm C}$ are the spin temperature of H I and the radio continuum background temperature, respectively. Note that the velocity-related term, $dv_{\rm LSR}/dr$, disappears in equation (7).

Using the integrated intensity maps from 85 to 105 km s^{-1}, we obtain maps of averaged $T_{\rm B}$ by dividing the intensity maps by the velocity width of 20 km s^{-1}. The averaged spin temperature at $l \sim 30^\circ$ was measured to be $T_{\rm S}$ ∼ 100 K (Sofue 2018). However, the observed brightness around G30.5 often exceeds this value, and we adopt here a spin temperature of $T_{\rm S} \simeq 130$ K as the maximum $T_{\rm B}$ in the map, which is considered to be saturated, and hence represents the spin temperature in the analyzed region. The background continuum brightness is assumed to be on the order of half of the observed brightness, and is measured to be $T_{\rm C} \sim 10$ K near the Galactic plane in the analyzed region (Sofue 2018), small enough compared to $T_{\rm S}$. Therefore, we neglect the continuum contribution, and approximate the optical depth by

$$\tau_{\rm HI} \simeq -\ln\left(1 - \frac{T_{\rm B:HI}}{T_{\rm S}}\right). \tag{11}$$

Note that this approximation does not hold toward strong continuum sources, but their areas are negligibly small compared to the analyzed region and do not affect the result significantly. Using this optical depth, we can calculate the H I density by equation (9).

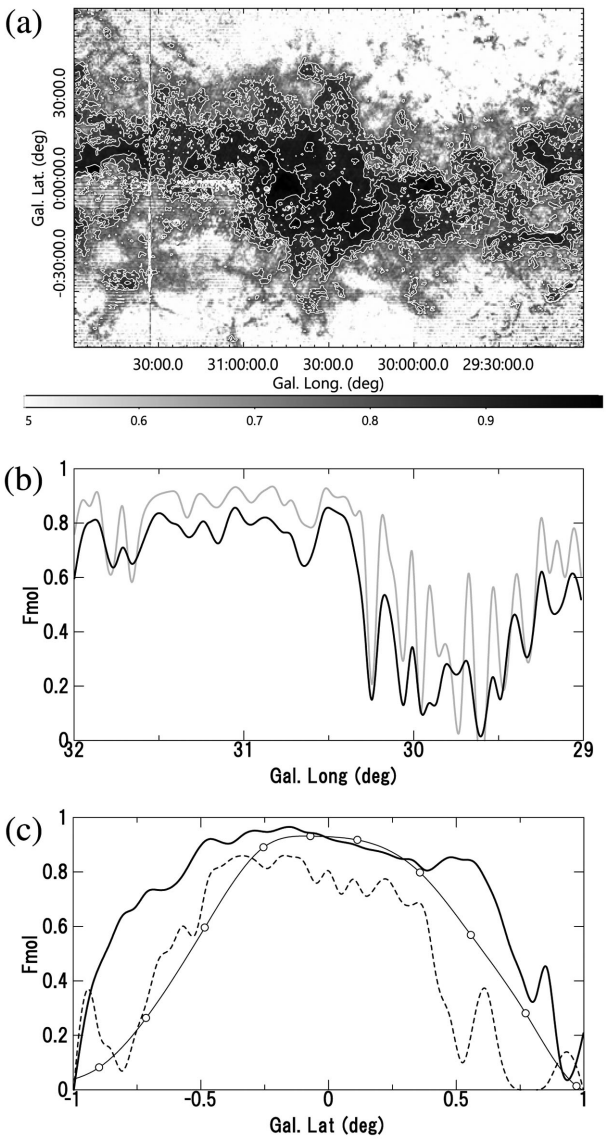

Fig. 10. (a) Molecular fraction $f_{\rm mol}$. In the molecular region, the fraction is almost saturated at $f_{\rm mol} \geq 0.8$, where contours are drawn every 0.05 from 0.8 to 0.95. The white regions are for $f_{\rm mol} \leq 0.5$. (b) Horizontal variation at $b = +0.^\circ5$ across the MBS, showing H I to H_2 transition at the MBS by the full line, and the same for the optically thin assumption in gray. A clear molecular front appears at the MBS front. (c) Vertical variations at $l = 29.^\circ5$ (dashed line) and $30.^\circ5$ (full line), showing full thickness of $0.^\circ9$ (87 pc) and $1.^\circ5$ (144 pc), respectively. The thin line is a global value at galactocentric radius 4 kpc taken from Sofue and Nakanishi (2016).

Figure 2c shows the obtained map of the optical depth. The volume density of H I is obtained by multiplying $X_{\rm HI} T_{\rm S} dv/dr$ to this map, which is representatively 7.8 H cm^{-3} for $T_{\rm S} = 130$ K and $dv/dr \sim 0.1$ km s^{-1} kpc^{-1}. Therefore, the typical value of $\tau \sim$ 2–3 yields ∼12–18 H cm^{-3}. Note that the values toward strong continuum sources brighter than 130 K (W 43, G29.96, etc.) are not valid, since the present approximation of low continuum background does not hold.

Figure 10b shows a map of $f_{\rm mol}$, and figures 10c and 10d are horizontal cross-sections at $b = +0.^{\circ}5$ and vertical at $l = 29.^{\circ}5$ and $30.^{\circ}5$, respectively. The figures show that the molecular fraction is saturated in the GMA and GMC at $f_{\rm ml} \geq 0.8$–0.9.

The horizontal cross-section at $b = 0.^{\circ}5$ (figure 10b) shows a sudden increase of $f_{\rm mol}$ making a sharp molecular front coincident with the MBS front. This fact shows that the H I gas is transformed to H_2 by the shock compression at the MBS front.

The separate structure between CO and H I is understood by transition of H I to H_2 at the MBS edge in a short timescale. The transverse velocity of the inflow of H I gas is on the order of $\delta V = (V_{\rm rot} - V_{\rm p})\sin p \sim 30\,{\rm km\,s^{-1}}$. Then the transition time is estimated to be $t \sim \lambda/\delta V \sim 3 \times 10^5$ yr, where $\lambda \sim 10$ pc is the width of the transition region, which may be approximated by the width of the molecular BS.

The constantly high molecular fraction of $f_{\rm mol} \sim 0.8$–0.9 near the Galactic plane manifests the global high molecular fraction in the inner Galaxy. A study of galactic-scale $f_{\rm mol}$ variation indicated $f_{\rm mol} \sim 0.8$–0.9 at $R \sim 4$ kpc within the molecular disk of thickness $\sim\pm 50$ pc (Sofue & Nakanishi 2016).

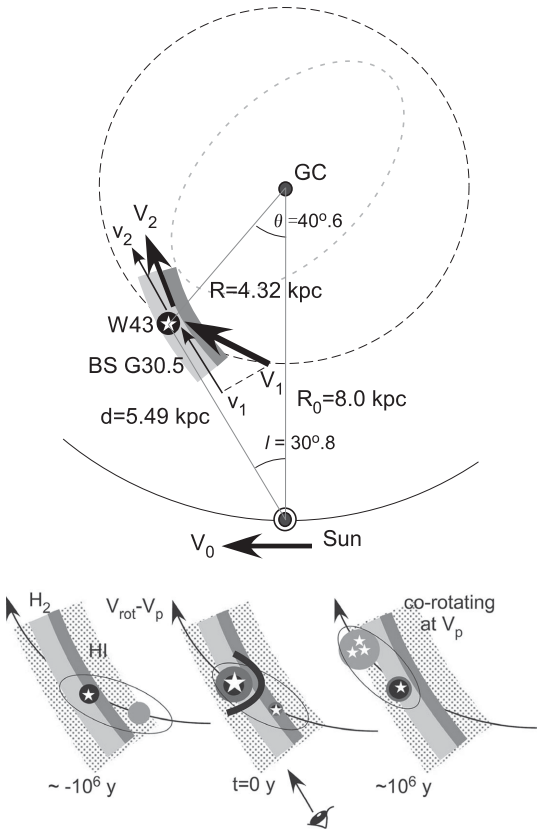

Fig. 11. (Top) Face-on location of the 4 kpc molecular arm near W 43 at a distance of 5.5 kpc, adopted from Zhang et al. (2014). The thick and narrow arrows indicate the gas flow and radial velocity, respectively. (Bottom) Chronological passage of the W 43 group ($t = 0$ y) in galactic rotation at $V_{\rm rot}$ through the Galactic shock wave corotating at the pattern speed $V_{\rm p}$ of the spiral potential. The sketch is in the corotating system at $V_{\rm p}$.

5 Discussion

5.1 Formation mechanism of a galactic bow shock

We first assume that the 4 kpc arm is the H I+H_2 spiral arm defined by Sofue and Nakanishi (2016) as Arm No. 4, which is identical to the Scutum arm of Sato et al. (2014), and W 43 Main, West, and G30.5 MBS are located along this arm.

Since there is no parallax for W 43 Main and G30.5, there remains a possibility that W 43 is far (~9 kpc) and G30.5 near (~5 kpc), or vice versa. However, the fact that the MBS has a clear arc structure concave to W 43 may be taken as evidence that they are physically interacting. So, we assume here that both W 43 Main and the MBS are on the same side, and, further, with the near side closer to G29.96 (West) in the same GMA.

Based on this assumption, we consider a possible scenario to explain the kinematics and three-dimensional molecular structure of the G30.5 MBS. As illustrated in figure 11, the upstream gas at velocity V_1 is accelerated toward the spiral potential well, where the gas is shocked, compressed, and decelerated to velocity V_2. The velocity direction is bent suddenly at the front and, accordingly, the projected line-of-sight (LSR) velocity is decelerated from up- to downstream sides.

By the bow shock and the hydraulic jump, the gas is also accelerated in the z direction, and is lifted to higher z. According to the loss of angular momentum by the interaction with the slowly rotating spiral potential at $V_{\rm p}$, the rotation velocity, $V_{\rm rot}$, of the shocked gas is decelerated. This results in a bow-like behavior in the v, b diagram (figure 5).

The velocity gradient (figure 4) at the bow front is as large as ~ -5 to $-10\,{\rm km\,s^{-1}}$ per ~10 pc, or ~ -50 to $-100\,{\rm km\,s^{-1}\,kpc^{-1}}$. This is significantly greater than the radial velocity gradient due to Galactic rotation, which is on the order of $\sim -10\,{\rm km\,s^{-1}\,kpc^{-1}}$. Thus, the velocity jump can be reasonably attributed to a specific change in the local flow velocities around the BS.

According to the scenario proposed here, W 43 and its molecular complex were formed prior to the encounter of the gas in the BS. This means, in turn, that the SF and molecular complex W 43 are being affected by the inflowing gas from the upstream side.

Although we assumed a spiral structure, we comment on a possible effect of the Galactic bar. The noncircular

motion parallel to the bar, apparently outward from the GC, would encounter the circular flow in the spiral arms (Teuben & Sanders 1985; Contopoulos et al. 1989; Kenney & Lord 1991). This may cause enhanced compression of the gas over the compression by spiral density wave, and the above scenario may work more efficiently.

5.2 Chronology in the 4 kpc arm

Based on the timescales estimated for the clouds and for the evolutionary stages of the H II regions, we try to present here a chronological view of the molecular complex centered on G30.8 embedding the H II regions and GMC.

5.2.1 Molecular association and clouds

From table 1 we find that the detected clouds (GMA, GMC, DMC, and cores) are gravitationally bound. However, the Jeans times indicate that only larger-sized clouds than the GMC can survive during the travel from one arm to the next. Smaller-sized and higher-density clouds such as dense MC and cores are unstable and collapse within a couple of Myr, and are considered to be formed rather recently inside the complex during the passage of the Galactic shock wave.

5.2.2 W 43 Main (G30.8)

The prominent H II region W 43 Main is embedded in a GMC with peak CO intensity as high as $I_{\mathrm{CO:peak}} \sim 500\,\mathrm{K\,km\,s^{-1}}$, and the age is ~1–5 Myr from stellar spectroscopy (Motte et al. 2003; Bally et al. 2010). The H I line absorption against the continuum begins coincident with the radial velocity of the GMC at G30.8, showing a clear association of the H II region with molecular gas. Thus, W 43 may be safely regarded to be the central source of the GMC and GMA.

Because the parallax of W 43 Main itself is not measured (Zhang et al. 2014; Sato et al. 2014), the accurate location on the line of sight is not known. The near-side distance for the recombination-line velocity $v_{\mathrm{LSR}} = 91.5\,\mathrm{km\,s^{-1}}$ indicates a closer distance of $r = 5.1$ kpc (Downes et al. 1980). Note that the value adopted here, 5.5 kpc, is the mean of those of G29.96, G29.86, G31.28, and G31.58.

A supersonic flow from the upstream side is encountering the eastern end of the W 43 GMC, where the gas is shocked and widened to high latitudes, and produces the bow structure. However, the shock wave may not be directly triggering the SF activity in W 43 Main. Instead, the shock at G30.5 is being formed by the encounter of the upstream edge of the GMC surrounding W 43 with the bow shock. Accordingly, a new dense MC is being formed at the root of the bow at G30.5−0.1 with peak intensity $\sim 400\,\mathrm{K\,km\,s^{-1}}$.

5.2.3 W 43 West (G29.96)

The age of G29.96 is estimated to be ~0.01–0.1 Myr (Watson et al. 1997; Beuther et al. 2007). It is associated with a dense GMC with peak intensity $\sim 500\,\mathrm{K\,km\,s^{-1}}$.

The line-of-sight distance is measured rather accurately to be 5.5 kpc from trigonometric parallaxes (Zhang et al. 2014), which is consistent with the recombination-line velocity $v_{\mathrm{LSR}} = 99.5\,\mathrm{km\,s^{-1}}$ (Downes et al. 1980). On the sky, G29.96 is located ~80 pc away from W 43 Main and ~50 pc from the bow shock at G30.5. In particular, the separation by 80 pc in the supersonic flow should not allow for W 43 Main and West to interact physically.

Therefore, chronologically, positionally, as well as gas-dynamically, W 43 West (G29.96) will not be physically related to W 43 Main, except that both belong to an extended GMA. Although some physical relation has been suggested between Main and West (Nguyen Luong et al. 2011), we will not argue for a further connection.

5.3 Multiple jumps and bows

The multiple step-like behavior of the disk thickness at G29.96, G30.5, G31.4, and G31.8 (figures 1 and 2) may be understood as a result of sequential inflow of supersonic gas from the upstream side. Figure 11 illustrates the chronological behavior of the molecular complex through the Galactic shock wave.

The inflowing molecular complex was shocked at its downstream side front and formed the GMC some Myr ago, in which W 43 was born. The complex with W 43 and its GMC in the center flew down to G30.8. The shock front propagated to the present place at G30.5, where a new GMC is being formed at its root. Another supersonic flow in the far upstream at G29.9 is now forming the dense molecular cloud at G29.96 and the ultra-compact H II region, which is also associated with a hydraulic jump.

According to the scenario drawn in figure 11, the two H II regions, W 43 Main and G29.96, are rotating approximately on the same orbit. They may be embedded in a GMA enclosed by contours at $I_{\mathrm{CO}} \sim 100\,\mathrm{K\,km\,s^{-1}}$ in figure 2c, which is gravitationally bound and can be sustained for several Myr as shown in table 1.

As listed in table 1, molecular structures less than dense MC sizes are also gravitationally bound systems, but their Jeans time is shorter than the arm-crossing time, so that they cannot remain from one arm to the other. On the other hand, the whole complex has a Jeans time comparable to the arm-crossing time, and can live for galactic time. Namely, the whole complex (GMA) is able to remain as a gravitationally bound system during the Galactic rotation from one arm to the other. More local condensations like

MCs and dense MCs, associated with SF, are formed during every passage through the Galactic shock wave.

We point out that the thickness jumps are mostly associated with vertically extended molecular bows, as recognized at G29.96, G30.5, G31.4, and G31.8, among which G30.5 is the most prominet and discussed here in detail. The bow at G31.8 extends toward much higher latitudes, reaching the edge of the observed region at $b \sim 1^\circ$ (± 100 pc). We may speculate that the molecular bow structures are commonly associated with molecular complexes formed in galactic shock waves.

5.4 Extragalactic giant cometary H II regions and molecular bow shocks

Giant cometary H II regions associated with inner-Hα-rimmed molecular bows are commonly found along borders between dark lanes and stellar-bright arms in spiral galaxies (Y. Sofue in preparation). The extragalactic dark bows are located on the upstream sides of OB associations along the arms and concave to the H II regions. The dark bows have bright inside rims in Hα emission illuminated by the central OB stars, making giant H II cones open to downstream of the galactic shock wave. The sizes are typically from $\sim$50 to $\sim$200 pc, depending on the luminosity of the central OB cluster as well as on the strength and density of the galactic shock wave.

Although the extragalactic bows are seen from outside the galactic plane, their similarity in shape and size is remarkable to the bow structure of MBS G30.5 seen edge-on in the Scutum arm of the Milky Way. We may consider that the MBS as studied here at G30.5 may be a common giant cometary phenomenon in spiral arms not only in the Galaxy but also in galaxies.

6 Summary

The ideal location of the molecular complex around W 43 (G30.8) near the tangent-velocity point of the Scutum arm (4 kpc arm) made it possible to investigate the three-dimensional structure of a galactic shock wave in the densest spiral arm of the Galaxy.

Using the FUGIN ^{12}CO($J = 1$–0) data cube, we measured the sizes, masses, densities, and Jeans times of the GMA, GMC, DMC, and molecular cores around G30.5, and listed the results in table 1.

The molecular complex at G30.5 is associated with a molecular bow shock (MBS) $\sim$100 pc long and $\sim$10 pc wide concave to W 43, which extends perpendicularly to the Galactic plane in positional coincidence with the radio continuum bow structure. The bow shape is reproduced well by a theoretical bow-shock model with a standoff distance of $\sim$50 pc from W 43.

The side edge on the upstream side of the MBS is extremely sharp, with a growth width of 0.5 pc indicative of a shock front property. The vertical disk thickness increases at the bow shock from lower to upper longitudes, indicating a hydraulic jump.

Based on these observations, we propose a formation scenario of the MBS, as illustrated in figures 8 and 11. The molecular gas in a GMA was condensed and accelerated by the Galactic spiral potential, and encountered the molecular complex around W 43 and the H II region, where a concave bow shock was formed.

We also showed that the H I gas has significant deficiency in the MBS and molecular regions. The molecular fraction suddenly increases and is saturated at $f_{\rm mol} \sim 0.9$ at the bow shock. Considering the Galactic rotation and flow of gas in the analyzed region, this may be evidence for H I to H_2 transition through the Galactic shock wave.

Acknowledgments

The authors are indebted to all the staff of NRO for their continuous support during the observations. The data analysis was partly carried out on the open-use data analysis computer system at the Astronomy Data Center of the National Astronomical Observatory of Japan.

References

Arce, H. G., & Goodman, A. A. 2002, ApJ, 575, 928
Altenhoff, W. J., Downes, D., Pauls, T., & Schraml, J. 1979, A&AS, 35, 23
Arthur, S. J., & Hoare, M. G. 2006, ApJS, 165, 283
Bally, J., et al. 2010, A&A, 518, L90
Baranov, V. B., Krasnobaev, K. V., & Kulikovskii, A. G. 1971, Soviet Phys. Doklady, 15, 791
Beuther, H., et al. 2012, A&A, 538, A11
Beuther, H., Zhang, Q., Bergin, E. A., Sridharan, T. K., Hunter, T. R., & Leurini, S. 2007, A&A, 468, 1045
Bialy, S., Burkhart, B., & Sternberg, A. 2017, ApJ, 843, 92
Bihr, S., et al. 2015, A&A, 580, A112
Bolatto, A. D., Wolfire, M., & Leroy, A. K. 2013, ARA&A, 51, 207
Carlhoff, P., et al. 2013, A&A, 560, A24
Contopoulos, G., Gottesman, S. T., Hunter, J. H., Jr., & England, M. N. 1989, ApJ, 343, 608
Downes, D., Wilson, T. L., Bieging, J., & Wink, J. 1980, A&AS, 40, 379
Dyson, J. E. 1975, Ap&SS, 35, 299
Fujimoto, M. 1968, in IAU Symp. 29, Nonstable Phenomena in Galaxies, ed. M. Arakeljan (Yerevan: Publishing House of the Academy of Sciences of Armenian SSR), 453.
Gómez, G. C., & Cox, D. P. 2004a, ApJ, 615, 744
Gómez, G. C., & Cox, D. P. 2004b, ApJ, 615, 758
Handa, T., Sofue, Y., Nakai, N., Hirabayashi, H., & Inoue, M. 1987, PASJ, 39, 709

Honma, M., Nagayama, T., & Sakai, N. 2015, PASJ, 67, 70
Kenney, J. D. P., & Lord, S. D. 1991, ApJ, 381, 118
Kohno, M., et al. 2018, PASJ, 70, S50
Kuijken, K., & Gilmore, G. 1989, MNRAS, 239, 605
Lin, Y., et al. 2016, ApJ, 828, 32
Martos, M. A., & Cox, D. P. 1998, ApJ, 509, 703
Motte, F., et al. 2014, A&A, 571, A32
Motte, F., Schilke, P., & Lis, D. C. 2003, ApJ, 582, 277
Nguyen Luong, Q., et al. 2011, A&A, 529, A41
Ogura, K. 1995, Ap&SS, 224, 151
Povich, M. S., Benjamin, R. A., Whitney, B. A., Babler, B. L., Indebetouw, R., Meade, M. R., & Churchwell, E. 2008, ApJ, 689, 242
Reich, W., Fuerst, E., Reich, P., & Reif, K. 1990, A&AS, 85, 633
Reid, M. J., & Ho, P. T. P. 1985, ApJ, 288, L17
Reipurth, B., Heathcote, S., Morse, J., Hartigan, P., & Bally, J. 2002, AJ, 123, 362
Roberts, W. W., Jr. 1972, ApJ, 173, 259
Sakemi, H., Machida, M., Akahori, T., Nakanishi, H., Akamatsu, H., Kurahara, K., & Farnes, J. 2018, PASJ, 70, 27
Saral, G., et al. 2017, ApJ, 839, 108
Sato, M., et al. 2014, ApJ, 793, 72
Sofue, Y. 1985, PASJ, 37, 507
Sofue, Y. 2013, PASJ, 65, 118
Sofue, Y. 2018, PASJ, 70, S50
Sofue, Y., & Nakanishi, H. 2016, PASJ, 68, 63
Steggles, H. G., Hoare, M. G., & Pittard, J. M. 2017, MNRAS, 466, 4573
Subrahmanyan, R., & Goss, W. M. 1996, MNRAS, 281, 239
Sugitani, K., Fukui, Y., & Ogura, K. 1991, ApJS, 77, 59
Teuben, P. J., & Sanders, R. H. 1985, MNRAS, 212, 257
Thompson, M. A., White, G. J., Morgan, L. K., Miao, J., Fridlund, C. V. M., & Huldtgren-White, M. 2004, A&A, 414, 1017
Tosa, M. 1973, PASJ, 25, 191
Ueta, T., et al. 2008, PASJ, 60, S407
Umemoto, T., et al. 2017, PASJ, 69, 78
Urquhart, J. S., Thompson, M. A., Morgan, L. K., & White, G. J. 2006, A&A, 450, 625
van Buren, D., Mac Low, M.-M., Wood, D. O. S., & Churchwell, E. 1990, ApJ, 353, 570
Watson, A. M., & Hanson, M. M. 1997, ApJ, 490, L165
Wilkin, F. P. 1996, ApJ, 459, L31
Zhang, B., et al. 2014, ApJ, 781, 89